Numerical simulation of partially coherent broadband optical imaging using the finite-difference time-domain method

İlker R. Çapoğlu,[1,*] Craig A. White,[1] Jeremy D. Rogers,[1] Hariharan Subramanian,[1] Allen Taflove,[2] and Vadim Backman[1]

[1]Biomedical Engineering Department, Northwestern University, 2145 Sheridan Road, Evanston, Illinois 60208, USA

[2]Electrical Engineering and Computer Science Department, Northwestern University, 2145 Sheridan Road, Evanston, Illinois 60208, USA

*Corresponding author: capoglu@ieee.org

Received December 20, 2010; revised March 5, 2011; accepted March 15, 2011; posted March 25, 2011 (Doc. ID 139711); published April 27, 2011

Rigorous numerical modeling of optical systems has attracted interest in diverse research areas ranging from biophotonics to photolithography. We report the full-vector electromagnetic numerical simulation of a broadband optical imaging system with partially coherent and unpolarized illumination. The scattering of light from the sample is calculated using the finite-difference time-domain (FDTD) numerical method. Geometrical optics principles are applied to the scattered light to obtain the intensity distribution at the image plane. Multilayered object spaces are also supported by our algorithm. For the first time, numerical FDTD calculations are directly compared to and shown to agree well with broadband experimental microscopy results.

OCIS codes: 050.1755, 110.0180.

Rigorous numerical electromagnetic methods are gaining more attention for characterizing, optimizing, and synthesizing optical systems in several areas of physics and engineering, including photolithography [1], integrated circuit inspection [2], and biophotonics [3]. One of the most popular of these methods is the finite-difference time-domain (FDTD) method [4], which provides a direct time-domain solution to Maxwell's equations by discretizing the electromagnetic field in both space and time. Compared to other prominent numerical electromagnetic methods, FDTD is very easy to implement and parallelize. In this Letter, we describe the full-vector FDTD numerical modeling of optical imaging systems with partially coherent, unpolarized illumination. In addition, our method supports planar multilayered object spaces, such as glass–air interfaces and silicon substrates of integrated circuits. The time-domain nature of FDTD also inherently supports broadband image formation.

An optical imaging system can conceptually be decomposed into four subcomponents: illumination, scattering, collection, and refocusing. The illumination and scattering subcomponents are shown in Fig. 1(a). The object to be imaged is placed in an FDTD grid, shown by the solid rectangle around the object. The illumination is introduced into the FDTD grid using the total-field/scattered-field (TF/SF) method [4]. In this method, the electric and magnetic fields of the illumination are only calculated on a closed surface called the TF/SF boundary, shown by the dashed rectangle in Fig. 1(a). The illumination scheme considered here is referred to as the Kohler illumination, shown on the left portion of Fig. 1(a). The light source on the left is imaged by an auxiliary lens on the aperture stop, situated on the front focal plane of the condenser lens. Light rays emanating from two mutually incoherent point sources L_1 and L_2 on the light source are represented by solid and dashed lines, respectively. The images of L_1 and L_2 on the aperture stop can also be assumed incoherent if the aperture stop is much larger than the Airy disk associated with the auxiliary lens [5]. For every image point on the aperture stop, the condenser lens creates an incident plane wave in its back focal plane. For an inhomogeneous source such as an arc lamp, these plane waves may have different amplitudes. The plane waves corresponding to L_1 and L_2 are shown by W_1 and W_2, respectively. Thus, Kohler illumination in its most ideal form is an incoherent summation of an infinite number of plane waves covering the numerical aperture $\mathrm{NA}_{\mathrm{ill}} = \sin(\theta_{\mathrm{ill}})$. Evidently, only a finite number of these plane waves can be employed in practice. An equally spaced arrangement of 88

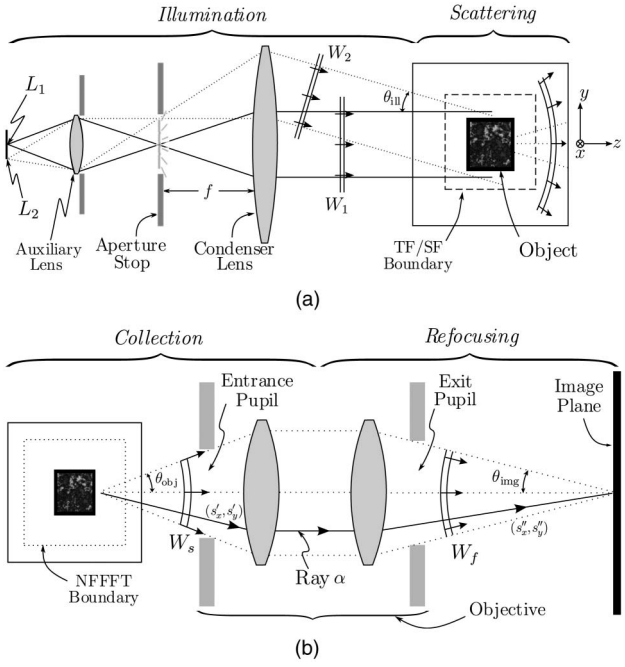

Fig. 1. Four subcomponents of an optical imaging system. (a) Illumination and scattering, (b) collection and refocusing.

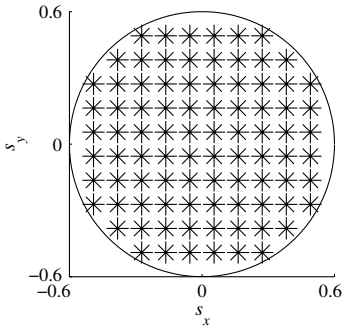

Fig. 2. Equally spaced arrangement of 88 plane waves for Kohler illumination with $\mathrm{NA_{ill}} = 0.6$. Two orthogonal polarizations (+) and (×) are shown for each direction of incidence.

plane waves in the direction-cosine space $(s_x, s_y) = (\sin\theta\cos\phi, \sin\theta\sin\phi)$ is shown in Fig. 2. Two orthogonal polarization states for each plane wave are denoted by (+) and (×). It will be explained shortly that these two states can always be chosen to be mutually incoherent; therefore, the *intensities* corresponding to each plane wave and each polarization state should be added to obtain the total intensity. In order to achieve this, every plane wave and every polarization should be simulated in a *separate* FDTD run. For the example in Fig. 2, 88 plane waves with two polarization states require 176 simulations in total. This is true for every deterministic numerical method in electromagnetics, time-domain, or frequency-domain.

The directions and weights of the orthogonal polarization states are determined by the polarization properties of the source image on the aperture stop. In addition to incoherence, we assume further that each point on the aperture stop is completely *unpolarized*, meaning that the two orthogonal polarization components at each point are completely incoherent [5]. As a result, *any* two equal-amplitude orthogonal polarization states can be chosen for the plane waves + and × in Fig. 2. If the source image on the aperture stop is partially polarized, the choice of these two mutually incoherent orthogonal polarization states is no longer arbitrary [6].

For each incident plane wave and polarization, the scattered near fields are calculated using FDTD, as shown in the right portion of Fig. 1(a). The near-field-to-far-field transform (NFFFT) [4] is then employed for calculating the far-zone radiated wavefront W_s in Fig. 1(b), using the near-field information on the NFFFT boundary shown by the dotted rectangle. This boundary is placed outside the dashed TF/SF boundary in Fig. 1(a) in order to collect only the scattered field from the object. The far field is calculated at discrete observation directions in an arrangement strictly analogous to that in Fig. 2, except that the directions are now inside the object-side numerical aperture $\mathrm{NA_{coll}} = \sin(\theta_{\mathrm{obj}})$. The far field corresponding to a multilayered medium is calculated in a fashion similar to that in [7], the only difference being frequency-domain operation. Assuming a well-corrected objective satisfying the Abbe sine condition, the direction cosines s'_x, s'_y of a particular ray entering the entrance pupil, denoted as α in Fig. 1(b), are reduced at the exit pupil by the *magnification* $M = \sin(\theta_{\mathrm{obj}})/\sin(\theta_{\mathrm{img}})$ of the objective. Neglecting chromatic aberrations, each ray on the wavefront W_f leaving the exit pupil also has the same frequency content as W_s. The $\hat{\theta}$ and $\hat{\phi}$ components (in the spherical coordinate system around $\hat{\mathbf{z}}$) of the electric field on each ray are also invariant [5]. Combining these facts with the vectorial diffraction theory, the final field distribution on the image plane is given by [8]

$$\mathbf{E}_{\mathrm{img}}(x,y) = -\frac{ik}{2\pi}\iint_{\Omega_{\mathrm{img}}} \mathbf{A}(s''_x, s''_y)\exp(ik(s''_x x + s''_y y))\mathrm{d}\Omega, \quad (1)$$

in which $k = \omega/c$, $(s''_x, s''_y) = (s'_x/M, s'_y/M)$ are the direction cosines at the exit pupil, Ω_{img} is the solid angle bounded by θ_{img}, $d\Omega = ds''_x ds''_y/s''_z = ds''_x ds''_y/\cos\theta$, and $\mathbf{A}(s''_x, s''_y)$ is the vectorial far-field amplitude of the ray at s''_x, s''_y. The integral in Eq. (1) can be evaluated using discrete methods such as two-dimensional FFT. The absolute square of $\mathbf{E}_{\mathrm{img}}(x,y)$ for each plane wave and polarization in Fig. 2 should be added to obtain the final image intensity.

The algorithm described thus far assumes narrowband operation. If a broadband solution is of interest, the FDTD grid is excited by a time pulse that contains the desired frequency band, and the response is calculated at the desired frequencies using the phasor-domain NFFFT [4]. The absolute square of this response can then be used for obtaining power spectral densities resulting from statistically stationary illuminations.

If the object space is multilayered, there exists a *scattered plane wave* corresponding to each incident plane wave. This plane wave is a result of the reflections from the layer boundaries and is considered "part of the incident wave" by the multilayer TF/SF plane-wave injector used in our algorithm [7]. It is therefore not collected by the NFFFT in Fig. 1(b). In order to propagate this wave to the image space, we first obtain its spectral content from the multilayer TF/SF plane-wave injector. We then trace the scattered plane wave through the collection refocusing system in Fig. 1(b) by keeping track of its direction cosines (s'_x, s'_y) and (s''_x, s''_y), as done above for the ray α. Finally, we add the scattered plane wave and the scattered field calculated by the NFFFT coherently at the image plane.

In Fig. 3, the spectral data obtained from microscopy experiments for two different sizes of polystyrene latex beads (2.1 and 4.3 μm diameter) placed on a glass slide ($n = 1.5$) are compared to numerical spectra calculated purely using FDTD. The experimental setup has $\mathrm{NA_{ill}} = 0.2$, $\mathrm{NA_{coll}} = 0.6$, and magnification $M = 40$. Details of the setup can be found in [9]. The parameters for the FDTD simulation are as follows: $5\,\mu\mathrm{m} \times 5\,\mu\mathrm{m} \times 5\,\mu\mathrm{m}$ grid with $\Delta x = \Delta y = \Delta z = 31\,\mathrm{nm}$, $\Delta t = (0.98/\sqrt{3})\Delta x/c$, and a 10-cell-thick convolutional perfectly matched layer. A total of 204 plane waves (102×2 polarizations) are sent within the first quadrant of the circle of illumination in Fig. 2, and the rotational symmetry of the bead is exploited to synthesize the final image. Each plane wave has a sine-modulated Gaussian waveform, whose −20 dB wavelengths are adjusted to coincide with the edges of the desired wavelength range. Both the measured/simulated spectra are normalized by the measured/simulated spectrum at a glass pixel. The plots on the left

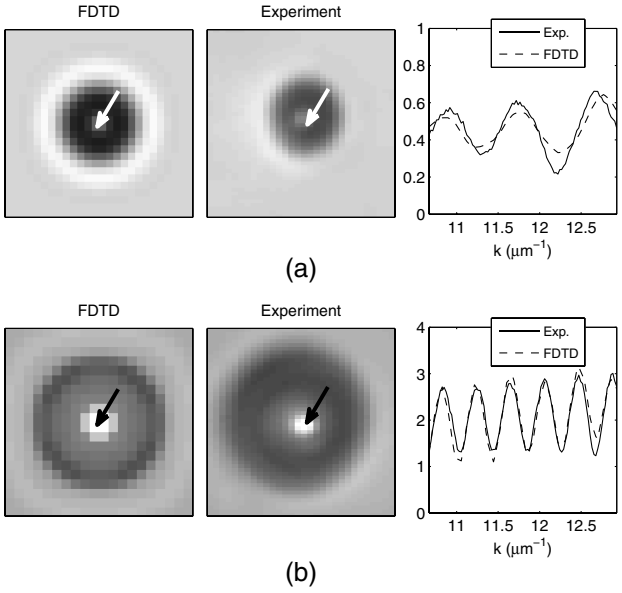

Fig. 3. Comparison of experimental results with FDTD calculations. (a) 2.1 μm bead, (b) 4.3 μm bead.

and center of Fig. 3 show the simulated and measured bright-field images in grayscale, respectively. The plots on the right in Fig. 3 show the measured and simulated spectra between 486 and 589 nm at the pixels annotated by arrows. In this wavelength range, the refractive index of the latex bead varies between 1.59 and 1.61. In the simulations, a fixed refractive index value of $n = 1.61$ is chosen as a first approximation. Modeling the exact dispersion relation can be an interesting extension to this comparison, but is outside our scope. Since the focusing depth in the measurement is unknown, a FDTD image at the optimum focusing depth is chosen for each comparison. At the optimum depth, the rms errors in the spectra are 11.4% and 8.2%, respectively. The frequency dispersion and the bead size variations are the most prominent contributors to this error.

Because of the air–glass interface, the simulation geometry is two-layered [10]. Therefore, the multilayer techniques mentioned earlier are used to illuminate the bead and collect the scattered light [7]. To illustrate the importance of this, the FDTD-simulated center-pixel reflectance spectrum for a bead suspended in free space is plotted in Fig. 4, together with the corresponding spectrum for a bead placed on a glass half-space. For better comparison, the reflection from the glass is subtracted coherently from the latter, as done in dark-field microscopy. Both spectra are normalized by the reflection from the glass half-space. The comparison clearly shows

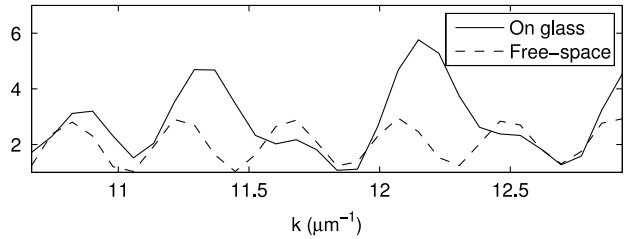

Fig. 4. Effect of the glass half-space below the bead on the reflectance spectrum at the center pixel.

that the glass half-space has a drastic effect on the reflectance spectrum, underlining the importance of the multilayer FDTD methods.

In this Letter, an FDTD-based algorithm for the full-vector numerical simulation of a broadband, partially coherent, unpolarized optical imaging system was described. Numerical results were shown to agree well with broadband experimental data for latex beads placed on a glass slide. Possible uses for this method include the calibration/design of optical systems and sample characterization.

This work was supported by National Institutes of Health (NIH) grants R01CA128641 and R01EB003682 and National Science Foundation (NSF) grant CBET-0937987.

References and Notes

1. D. C. Cole, E. Barouch, E. W. Conrad, and M. Yeung, Proc. IEEE **89**, 1194 (2001).
2. A. R. Neureuther, Microelectron. Eng. **17**, 377 (1992).
3. J. L. Hollmann, A. K. Dunn, and C. A. DiMarzio, Opt. Lett. **29**, 2267 (2004).
4. A. Taflove and S. C. Hagness, *Computational Electrodynamics: the Finite-Difference Time-Domain Method*, 3rd ed. (Artech House, 2005).
5. M. Born and E. Wolf, *Principles of Optics*, 7th ed. (Cambridge University Press, 1999).
6. J. Tervo, T. Setälä, and A. T. Friberg, J. Opt. Soc. Am. A **21**, 2205 (2004).
7. I. R. Capoglu, "Techniques for handling multilayered media in the FDTD method," Ph.D. thesis (Georgia Institute of Technology, 2007).
8. P. Török, P. R. T. Munro, and E. E. Kriezis, Opt. Express **16**, 507 (2008).
9. Y. Liu, X. Li, Y. L. Kim, and V. Backman, Opt. Lett. **30**, 2445 (2005).
10. Because of the finite illumination NA, the bottom interface is far out of focus. The reflection from that interface is spread over a large area, with much reduced intensity at the top interface. We therefore neglect the presence of the bottom interface and assume a two-layered geometry.